Journal of Neural Engineering

PURPOSE-LED PUBLISHING™

PAPER

Eccentricity confound in EEG-based visual attention decoding from gaze-fixated neural tracking of motion in natural videos

To cite this article: Yuanyuan Yao *et al* 2026 *J. Neural Eng.* **23** 056024

View the article online for updates and enhancements.

You may also like

- Identifying temporal correlations between natural single-shot videos and EEG signals
Yuanyuan Yao, Axel Stebner, Tinne Tuytelaars et al.
- A comparison study of visually stimulated brain–computer and eye-tracking interfaces
Kaori Suefusa and Toshihisa Tanaka
- A passive BCI for monitoring the intentionality of the gaze-based moving object selection
Darisy G Zhao, Anatoly N Vasilyev, Bogdan L Kozyrskiy et al.

This content was downloaded from IP address 134.58.253.56 on 25/09/2026 at 09:28

Journal of Neural Engineering

Check for updates

PAPER

RECEIVED
24 April 2026

REVISED
18 August 2026

ACCEPTED FOR PUBLICATION
6 September 2026

PUBLISHED
18 September 2026

Eccentricity confound in EEG-based visual attention decoding from gaze-fixated neural tracking of motion in natural videos

Yuanyuan Yao[1,*], Celina Salamanca González[1], Simon Geirnaert[1,2], Céline R Gillebert[3,5], Tinne Tuytelaars[4] and Alexander Bertrand[1]

[1] KU Leuven, Department of Electrical Engineering, STADIUS Center for Dynamical Systems, Signal Processing and Data Analytics, Leuven, Belgium
[2] KU Leuven, Department of Neurosciences, Research Group ExpORL, Leuven, Belgium
[3] KU Leuven, Brain and Cognition, Leuven, Belgium
[4] KU Leuven, Department of Electrical Engineering, Processing Speech and Images (PSI), Leuven, Belgium
[5] Leuven Brain Institute (LBI), Leuven, Belgium
[*] Author to whom any correspondence should be addressed.

E-mail: yuanyuan.yao@kuleuven.be

Keywords: visual attention decoding, EEG, neural tracking, gaze fixation, eccentricity confound

Abstract

Objective. Decoding visual attention from brain signals during naturalistic video viewing has emerged as a new direction in brain–computer interface research. Current methods assume that stronger coupling between object motion and neural activity indicates higher attention, but this can be confounded by eye movement artifacts and stimulus properties. This study investigates how visual eccentricity—the distance between a visual object and the fixation point—affects neural responses when eye movement artifacts are controlled. *Approach.* Electroencephalography (EEG) signals were recorded across three tasks that manipulated object eccentricity and attention conditions while participants maintained gaze fixation. Correlation analysis and match-mismatch decoding were performed to quantify the neural tracking of object motion. *Main results.* The analysis supports three conclusions: (1) neural tracking of object motion in natural videos works under gaze fixation; (2) the strength of this tracking under gaze fixation is modulated by attention; and (3) there exists a significant eccentricity confound in the EEG responses, with poorer neural tracking of motion at larger eccentricities. *Significance.* These results indicate that findings from previous free-viewing studies also reflect genuine neural processing rather than mere oculomotor artifacts. However, the identified eccentricity effect highlights a major limitation for current decoding approaches that assume coupling strength reflects attention levels alone.

1. Introduction

Neural activity is modulated by attention: neurons processing task-relevant information exhibit increased firing rates and reduced variability, while those processing irrelevant information are suppressed [1]. This enhancement is likewise reflected in non-invasive, population-level electrophysiology, where the sensory-evoked response to an attended stimulus is amplified [2]. While such effects are typically quantified as the amplitude of a time-locked evoked response, the same enhancement can be captured by modeling the ongoing relationship between the stimulus and the neural response, where it appears as stronger temporal coupling between the two [3, 4]. This coupling has been observed not only with simple synthetic stimuli but also with naturalistic speech, images, and videos [5–8].

However, attention is not the only factor that influences stimulus-brain coupling strength. When using naturalistic stimuli, various confounding factors can modulate this coupling. For example, Li *et al* [9] reconstructed speech envelopes from electroencephalography (EEG) signals and used the correlation between reconstructed and actual envelopes as a metric for auditory attention. While this score was higher when participants were attentive and lower during distraction, it also correlated with the time-varying standard deviation of the speech envelope, suggesting that the score was also sensitive to stimulus dynamics rather than attention alone. When this confound was not addressed, decoding performance deteriorated.

© 2026 IOP Publishing Ltd. All rights, including for text and data mining, AI training, and similar technologies, are reserved.

This exemplifies that stimulus-brain coupling is not a pure measure of top–down goal-directed attention, but is also dependent on bottom–up sensory stimulus properties [10, 11]. Moreover, such bottom–up influences may not cancel out in complex naturalistic conditions and could systematically bias decoding results in real-world applications.

These concerns extend naturally to newly emerging EEG-based visual attention decoding paradigms with potential applications in education, neuromarketing, and clinical diagnostics [7, 8, 12]. We hypothesize that the spatial location of visual objects relative to gaze position (i.e. eccentricity, calculated from the center of the object's bounding box) could be a potential confound: a higher stimulus-brain coupling may not necessarily indicate higher attention, but could also result from the object being located at a more central location in the visual field. This is motivated by the well-established nonuniformity of visual processing, with maximal visual acuity and pattern recognition capabilities at the foveal and a rapid decline toward the periphery [13, 14]. A direct link between eccentricity and neural responses has been demonstrated previously. For instance, in a functional magnetic resonance imaging study by Wang *et al* [15], participants were presented with images of different categories (faces, houses, etc) at different eccentricity positions. They reported that the neural activation was most intense when stimuli were in the central visual field, and the magnitude of responses declined as eccentricity increased.

Beyond these stimulus-dependent effects, eye movements present another persistent confound in free-viewing paradigms. Under natural conditions, attention is typically accompanied by overt behavior such as directing gaze toward the attended object, which is known as overt attention. This is particularly relevant for paradigms relying on the motion information in naturalistic videos, as eye movements (saccades and smooth pursuit) are naturally evoked by the movements in the videos, and thus may strongly correlate with the video motion features. These eye movements can influence stimulus-EEG correlations through several mechanisms: (1) (residual) electrooculogram (EOG) artifacts in the EEG signals, (2) neural motor activity associated with the planning and execution of eye movements, and (3) neural responses to gaze-induced visual motion, akin to a moving-camera effect where the eyes serve as the camera. This ambiguity undermines findings from prior studies that reported significant neural tracking of video motion under free-viewing conditions [7, 8], since it remains unclear to what extent these effects reflect genuine neural processing of motion information rather than oculomotor contributions. In [12], eye gaze data were explicitly shown to be correlated with video motion features, and using gaze data alone could achieve comparable attention decoding performance to EEG-based decoders, which again raises concerns about the neural origin of the reported effects. Similarly, Ki *et al* [16] showed that the neural responses are spatially selective and are enhanced for task-related locations, but since their paradigm relied on overt attention, doubts remain as to whether the reported enhancement was simply an artifact of eye gaze bias toward task-relevant locations, rather than a genuine neural correlate of covert attentional selection.

Since disentangling genuine neural correlates of attention from oculomotor confounds is particularly challenging under free-viewing conditions, we follow a common strategy in cognitive neuroscience: employing a covert attention paradigm. Participants maintain fixation while attending to stimuli in the visual periphery, thereby eliminating eye-movement confounds at the cost of reduced ecological validity. This approach is well established: sustained covert attention to peripheral locations reliably modulates early visual responses, and can even be split across multiple non-contiguous peripheral targets [17]. This controlled approach allows us to rigorously test two key questions: (1) whether neural tracking of video motion persists in the absence of eye movement contributions, and (2) whether eccentricity of visual stimulation systematically influences this tracking.

The remainder of this paper is organized as follows. Section 2 describes the experimental protocol, including visual stimuli, tasks, and data acquisition. Section 3 details preprocessing and correlation analysis methods. Section 4 presents results on the effects of attention and eccentricity on single-subject decoding performance and inter-subject correlation (ISC). Section 5 discusses the implications of our findings. Finally, section 6 concludes the paper.

2. Experimental protocol

14 healthy young adults (6 men, 8 women), primarily university students, participated in the study, each providing written informed consent. All participants had normal or corrected to normal vision and confirmed they had no history of neurological diseases. Three visual attention tasks were designed to investigate the effects of attention and eccentricity confounds. The study was conducted in accordance with the ethical principles of the Declaration of Helsinki, and was approved by the KU Leuven Social and Societal Ethics Committee (Application G-2022-4765-R3).

2.1. Visual content

The stimuli consisted of seven single-shot natural videos taken from the video set used in [8, 12]. Each video featured a person performing a stage act and was truncated to 3 min duration with a frame rate of 30 Hz. To better control the performer's eccentricity relative to the gaze fixation point, we

centered the performer in each video by (1) detecting the performer's bounding box in each frame using a pre-trained Mask R-CNN model [18][6], (2) defining the bounding box size as the maximum width and height across all frames, (3) smoothing the bounding box center positions to reduce abrupt movements, and (4) cropping the video frames based on the smoothed centers and fixed bounding box size. The resulting cropped videos varied in size and were resized, with aspect ratios preserved, to a height of 540 pixels for display on a 1920 × 1080 pixel canvas with a black background. Given the display geometry (section 2.3), 540 pixels subtended approximately 6° of visual angle in height. While the stimulus width varied across individual videos to preserve the original aspect ratios of the cropped bounding boxes, it remained close to the height, with its horizontal visual angle ranging from 6° to 7°.

Three tasks were designed (see section 2.2), and the same seven videos were used in all three tasks. In Tasks 1 and 2, each cropped video gradually shifted from the screen center toward either the left or right side at a constant speed of 0.1 pixels per frame. In contrast, the videos in Task 3 remained centered (see figure 2). Because spatial direction was not an experimental factor of interest, the direction of the shift in Tasks 1 and 2 was treated as a nuisance variable and randomly assigned to prevent systematic directional bias. At this constant speed, and with a frame rate of 30 frames per second, each video's center translated a maximum of 540 pixels from the screen center over the 3 min duration. At maximum displacement, the video occupied the visual field from roughly 3° to 9° eccentricity (inner edge to outer edge, respectively).

Throughout all tasks and videos, a fixation cross (60 × 60 pixels) was presented at the screen center. Its luminance decreased and returned to normal at irregular intervals. Additionally, a red circle (radius: 50 pixels) appeared and faded out at random times and at random locations within each cropped video. An example frame with a circle appearing is shown in figure 1. These two visual events never occurred simultaneously, and each of these fade-out events lasted 2 s to avoid inducing strong time-locked event-related potentials. To keep participants engaged, they were instructed to respond to these two different types of events in different tasks (see section 2.2). The timing of these event onsets relative to each video was identical for all participants. During the eccentric videos in Tasks 1 and 2, consecutive crosses appeared on average every 19.9 s (range 10.1–42.4 s) and consecutive circles every 24.1 s (range 10.0–59.4 s). Events were sparser during the central videos in Task 3, with consecutive crosses spaced an average of 44.0 s apart (range 10.6–89.1 s) and consecutive circles spaced 39.3 s apart (range 10.3–100.8 s). For both conditions, these intervals were highly variable, ensuring that the appearance of crosses and circles remained temporally unpredictable rather than rhythmic. Because these event sequences were fixed per condition, every participant experienced the exact same total number of events throughout the experiment: 64 cross fade-outs and 43 circle events in Tasks 1 and 2, and 22 cross fade-outs and 21 circle events in Task 3.

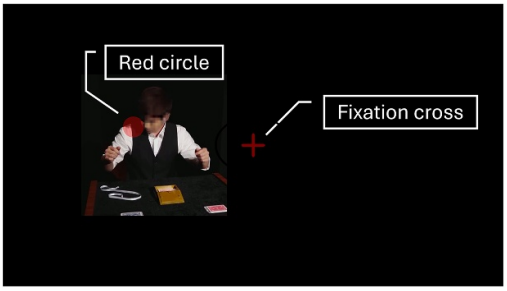


Figure 1. Illustration of a frame showing the central fixation cross and a red circle appearing at a random location in the video. The face is blurred for identification protection.

Each video was prefaced with instruction frames. The seven edited videos were then concatenated into a single 21 min (excluding instructions and questions) video per task, resulting in a total of 63 min of experimental data per participant. Because the same seven videos appeared in all three tasks, stimulus familiarity could accumulate across tasks. Therefore, both the task order and the video order within each task were randomized across participants to distribute any such effect across the three conditions rather than confounding a specific contrast. A full list of the task and video orders for each participant is provided in the appendix (table 3).

2.2. Tasks

Participants were instructed to maintain fixation on the central cross throughout all tasks. In Task 1 (ignore condition), they were instructed to ignore the video content. To discourage attending to the video, they were also instructed to press the '+' key with their preferred hand on a keyboard whenever the fixation cross dimmed. In Tasks 2 and 3 (attend conditions), participants attended to the videos while continuing to fixate. Because object eccentricity varies in Task 2 but remains constant in Task 3, the latter serves as a control to isolate the effects of eccentricity. To maintain consistent engagement with the video content, participants performed a vigilance task requiring them to press the 'o' key with their preferred hand whenever a subtle red circle appeared

[6] The Mask R-CNN model used an Inception v2 backbone with pre-trained weights from the COCO (Common Objects in Context) dataset. The model exhibited an exceptionally low bounding-box detection failure rate on our experimental stimuli (ranging from 0% to 1.46% across videos, mean = 0.24%). Missing bounding boxes in these frames were resolved via linear interpolation.

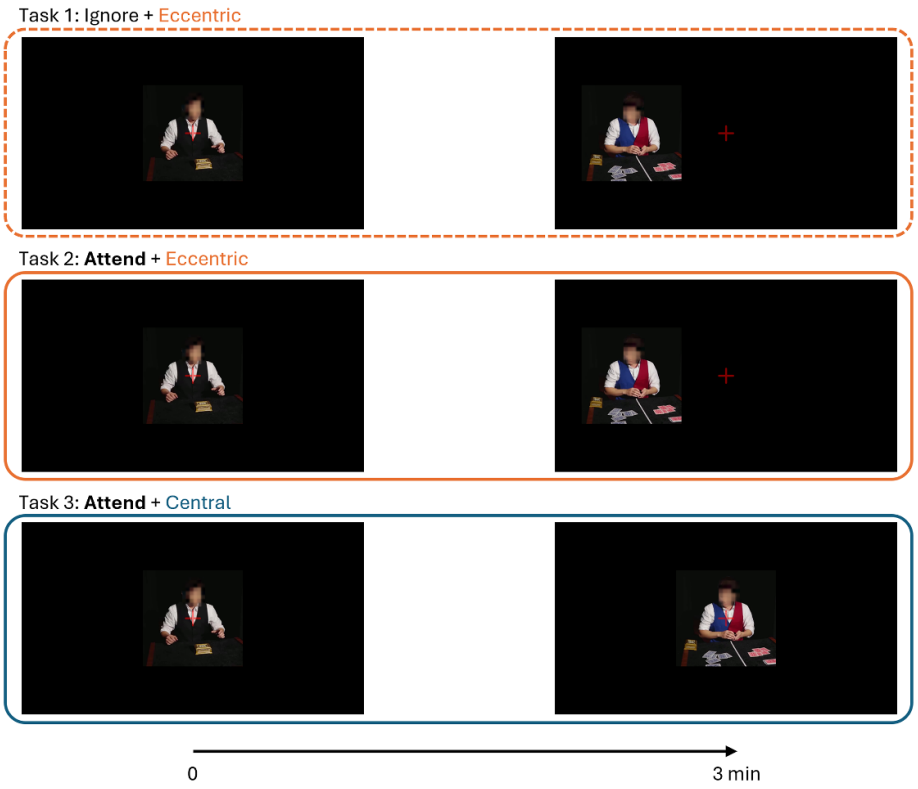


Figure 2. Illustration of the three experimental tasks. The faces are blurred for identification protection. In Task 1, participants ignored the videos while fixating centrally as the videos moved to the periphery. In Task 2, they attended to the videos while fixating centrally as the videos moved to the periphery. In Task 3, they attended to the videos while fixating centrally with the videos remaining in the center. Note that the foreground video does not always have a black or dark background as shown in this example.

Table 1. Summary of experimental tasks.

Task	Attention	Eccentricity	Gaze	Response trigger	Response
Task 1	Ignore	Central to peripheral	Fixed	Fixation cross dimming	Press '+' key
Task 2	Attend	Central to peripheral	Fixed	Red circle appearance	Press 'o' key
Task 3	Attend	Central	Fixed	Red circle appearance	Press 'o' key

within the video. The circle was kept deliberately subtle to minimize the chance of detecting it without attending to the video content, while a more salient target could also have competed with it. Both detection tasks served only to sustain engagement, and the key presses were not logged. The rationale and its limitations are discussed in section 5.5. An illustration of the attention and eccentricity conditions across the three tasks is shown in figure 2, and a summary of the tasks is provided in table 1.

2.3. Data acquisition

Stimuli were presented on a 22-inch monitor (1920 × 1080, 60 Hz refresh rate). Participants sat approximately 130 cm from the screen and were instructed to maintain a stable posture and minimize head and body movements during video playback.

EEG data were recorded using a 64-channel BioSemi ActiveTwo system at 2048 Hz. Four EOG electrodes were placed above/below the right eye and at the outer canthi of both eyes. During data acquisition, signal quality was monitored in real time via visual inspection of the signal traces. Channels were manually logged as bad if they displayed clear, irremediable artifacts. These included excessive high-frequency noise, severe signal drifts (often indicating unstable electrode contact), or flat signals typically resulting from conductive gel bridges between adjacent electrodes. Video onset was synchronized with EEG using a photodiode placed at the top-right corner of the screen, which detected a black-to-white box transition at the start of each video. This area was covered with black tape to avoid distracting the participants.

Gaze data were recorded using the Pupil Labs NEON eye tracker (200 Hz). A world-facing camera recorded the screen content from the participant's perspective. Gaze-video synchronization was achieved using a QR code embedded in the instruction frames. The time point when the QR code disappeared in the world-facing camera recording was

marked as video onset, and gaze timestamps were aligned to this reference point. Four reference markers were placed around the physical monitor. The Pupil Cloud Marker Mapper algorithm, which uses the world-facing camera to continuously detect these markers and define a static 2D surface corresponding to the screen, allowed us to export normalized, screen-relative gaze positions that are robust to head movements.

3. Methods

3.1. Preprocessing

The EEG and EOG data were preprocessed using standard techniques as in Yao *et al* [8]: segmentation based on photodiode synchronization signals, bad channel interpolation, average referencing, high-pass filtering (0.5 Hz cutoff), and notch filtering (50 Hz). The EOG data were then linearly regressed out from EEG to suppress ocular artifacts. All data were downsampled to 30 Hz with anti-aliasing to match the video frame rate. Rather than using raw video data, we extracted the object-based optical flow, which is a feature that quantifies the overall motion of a single object[7] in the video at each moment in time, resulting in a 1D time series with the same length as the original video [8]. The EEG signals and video features were centered to have zero mean per video.

Gaze coordinates, along with blink and saccade annotations, were exported from the eye tracker to identify non-fixation periods. First, gaze coordinates were clustered with the density-based spatial clustering algorithm DBSCAN [19], which is well suited for identifying dense fixation regions without requiring a predefined number of clusters. DBSCAN was run on the on-screen gaze coordinates (in pixels) with a neighborhood radius eps = 10 pixels and a minimum of 5 samples per core point (minPts = 5). The largest cluster, corresponding to the most frequently viewed region, was interpreted as the fixation cluster. To verify the physiological validity of these clusters, we calculated the 95th percentile radius from the cluster centroid, yielding an average fixation radius of approximately 1.22° of visual angle across all tasks (table 2). This aligns well with standard thresholds for human foveal vision. Samples falling outside this cluster were classified as non-fixations, except when blink annotations indicated that the deviation was caused by an eye blink. Saccade annotations served as a secondary check for non-fixation samples identified by DBSCAN. Any sample annotated as a saccade was categorized as a non-fixation, overriding its cluster assignment. An example of the gaze samples and the resulting fixation cluster for a representative participant in Task 1 is shown in figure 3. The mean and

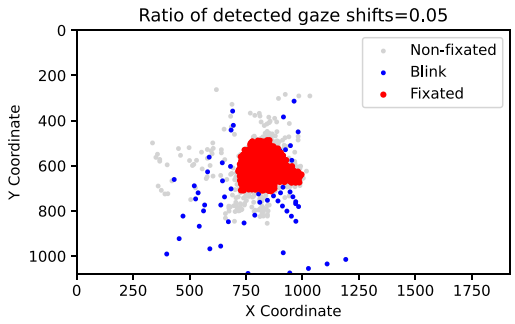


Figure 3. Illustration of non-fixation detection for a representative participant (subject 4) during a video in Task 1. Dots indicate gaze positions with colors representing fixations (red), eye blinks (blue), and non-fixations (gray).

standard deviation of the proportion of detected gaze shifts across participants and videos for each task are summarized in table 2.

From table 2, we conclude that the overall percentage of non-fixation samples is low, with Task 2 exhibiting a slightly higher proportion of gaze shifts. This increase may be attributable to the greater difficulty of maintaining central fixation when the attended object moves toward the periphery.

3.2. Correlation analysis

Two types of correlation analyses were performed: (1) stimulus-response correlation between EEG and video stimuli within each individual participant using canonical correlation analysis (CCA) [8], and (2) ISC of EEG responses across participants using correlated component analysis (CorrCA) [20]. For completeness, we briefly summarize both methods here.

Denote the EEG signals as $\mathbf{X} \in \mathbb{R}^{T\times D_x}$ and video stimuli as $\mathbf{Y} \in \mathbb{R}^{T\times D_y}$, where T is the number of samples, D_x is the number of EEG channels, and D_y is the dimension of the video features. In our case $D_x = 64$ as we collected 64-channel EEG, and $D_y = 1$ as we used the 1-dimensional object-based optical flow feature. However, these dimensions were expanded by adding time-lagged copies of the signals, enabling a data-driven temporal alignment between the two modalities and realizing a data-driven finite impulse response filtering that suppresses irrelevant frequency bands. Specifically, including $L_x - 1$ time lags together with an offset Δ_x that accounts for latencies between the EEG and the stimulus signal for an EEG sample $\mathbf{X}(t) = [x_1(t), \ldots, x_{D_x}(t)] \in \mathbb{R}^{1\times D_x}$ yields the extended vector:

$$\begin{aligned}\tilde{\mathbf{X}}(t) = [&x_1(t+\Delta_x), x_1(t-1+\Delta_x), \ldots,\\ &x_1(t-L_x+1+\Delta_x), \ldots, x_{D_x}(t+\Delta_x),\\ &x_{D_x}(t-1+\Delta_x), \ldots, x_{D_x}(t-L_x+1+\Delta_x)]\\ &\times \in \mathbb{R}^{1\times D_x L_x}. \end{aligned} \quad (1)$$

The inclusion of this fixed offset Δ_x is particularly useful to compensate for a delay in the neural

[7] The videos in our experiment only contain one object, namely the human performer.

Table 2. Gaze shift and fixation cluster statistics across participants and videos per task. The table presents the mean and standard deviation for the percentage of samples classified as gaze shifts, as well as the radius of the primary fixation cluster. The fixation radius is expressed in degrees of visual angle (DVA).

	Percentage of detected gaze shift samples		Fixation cluster radius (DVA)	
Task	Mean (%)	Std (%)	Mean (°)	Std (°)
Task 1 (ignore, eccentric)	3.7	3.3	1.21	0.32
Task 2 (attend, eccentric)	5.9	5.6	1.23	0.31
Task 3 (attend, central)	3.6	3.5	1.21	0.33

response to the video while avoiding the introduction of a large number of time lags, which would unnecessarily expand the dimension of $\mathbf{X}$ and $\mathbf{Y}$. A similar operation, with $L_y - 1$ time lags and offset Δ_y, was applied to the video features. After this extension, the dimensions of $\mathbf{X}$ and $\mathbf{Y}$ became $T \times D_x L_x$ and $T \times D_y L_y$, respectively.

Recall that the signals were centered to have zero mean. The CCA model finds linear maps $\mathbf{w_x}$ and $\mathbf{w_y}$ such that the correlation between the transformed signals is maximized [21]:

$$\begin{aligned} \underset{\mathbf{w}_x, \mathbf{w}_y}{\text{maximize}} \quad & \mathbf{w}_x^{\mathrm{T}} \mathbf{X}^{\mathrm{T}} \mathbf{Y} \mathbf{w}_y \\ \text{subject to} \quad & \mathbf{w}_x^{\mathrm{T}} \mathbf{X}^{\mathrm{T}} \mathbf{X} \mathbf{w}_x = 1, \\ & \mathbf{w}_y^{\mathrm{T}} \mathbf{Y}^{\mathrm{T}} \mathbf{Y} \mathbf{w}_y = 1. \end{aligned} \tag{2}$$

The optimized $\mathbf{w_x}$ and $\mathbf{w_y}$ are the first canonical components, yielding the first canonical directions $\mathbf{X}\mathbf{w_x}$ and $\mathbf{Y}\mathbf{w_y}$. A higher correlation between these canonical directions indicates stronger neural tracking of the video features.

Higher-order components can be obtained by solving the same optimization problem with an additional constraint that these higher-order canonical directions are orthogonal to all previous canonical directions. Aggregating canonical components from first to Kth order as $\mathbf{w_x} \in \mathbb{R}^{D_x L_x \times K}$, $\mathbf{w_y} \in \mathbb{R}^{D_y L_y \times K}$, the solution can be obtained by solving a generalized eigenvalue decomposition (GEVD) problem:

$$\begin{aligned} \mathbf{R}_{xy} \mathbf{R}_{yy}^{-1} \mathbf{R}_{yx} \mathbf{w_x} &= \mathbf{R}_{xx} \mathbf{w_x} \mathbf{\Lambda}, \\ \mathbf{R}_{yx} \mathbf{R}_{xx}^{-1} \mathbf{R}_{xy} \mathbf{w_y} &= \mathbf{R}_{yy} \mathbf{w_y} \mathbf{\Lambda}, \end{aligned} \tag{3}$$

where $\mathbf{R}_{xy} = \mathbf{X}^{\mathrm{T}}\mathbf{Y}$, $\mathbf{R}_{yx} = \mathbf{Y}^{\mathrm{T}}\mathbf{X}$, $\mathbf{R}_{xx} = \mathbf{X}^{\mathrm{T}}\mathbf{X}$, $\mathbf{R}_{yy} = \mathbf{Y}^{\mathrm{T}}\mathbf{Y}$, and $\mathbf{\Lambda}$ is a diagonal matrix with eigenvalues in descending order.

CorrCA extends CCA to a group-level analysis, enabling the extraction of common neural components from the EEG data of multiple (more than two) participants. Since the EEG signals of all participants are time-locked on the same videos, these common components are expected to be neural responses to these videos [20]. Using subscript n to denote the subject index, EEG signals from different subjects are denoted as $\mathbf{X}_n$, where $n = 1, \ldots, N$. CorrCA finds a shared[8] spatial filter $\mathbf{W}_s$ that maximizes the approximate average pairwise correlations between all subject pairs:

$$\begin{aligned} \underset{\mathbf{W}_s}{\text{maximize}} \quad & \sum_{i=1, i\neq j}^{N} \sum_{j=1}^{N} \mathrm{Tr}\left(\mathbf{W}^{\mathrm{T}}{}_s \mathbf{R}_{ij} \mathbf{W}_s\right) \\ \text{subject to} \quad & \sum_{i=1}^{N} \mathbf{W}^{\mathrm{T}}{}_s \mathbf{R}_{ii} \mathbf{W}_s = \mathbf{I}_K, \end{aligned} \tag{4}$$

where $\mathrm{Tr}(\cdot)$ denotes the trace, $\mathbf{W}_s$ contains the first K canonical components, and $\mathbf{R}_{ij} = \mathbf{X}^{\mathrm{T}}{}_i \mathbf{X}_j$ is the cross-covariance matrix between participants i and j. This optimization problem can also be solved via a GEVD:

$$\left(\sum_{i=1}^{N}\sum_{j=1}^{N} \mathbf{R}_{ij}\right) \mathbf{W}_s = \left(\sum_{i=1}^{N} \mathbf{R}_{ii}\right) \mathbf{W}_s \mathbf{\Lambda}. \tag{5}$$

The eigenvalues in $\mathbf{\Lambda}$ are in descending order. ISC for the kth component is defined as the average correlation between all subject pairs:

$$\mathrm{ISC}_k = \frac{2}{N(N-1)} \sum_{i=1}^{N} \sum_{j=i+1}^{N} \frac{\mathbf{W}^{\mathrm{T}}{}_{s,k} \mathbf{R}_{ij} \mathbf{W}_{s,k}}{\sqrt{\mathbf{W}^{\mathrm{T}}{}_{s,k} \mathbf{R}_{ii} \mathbf{W}_{s,k}} \sqrt{\mathbf{W}^{\mathrm{T}}{}_{s,k} \mathbf{R}_{jj} \mathbf{W}_{s,k}}}, \tag{6}$$

where $\mathbf{W}_{s,k}$ is the kth column of $\mathbf{W}_s$. Higher ISC indicates stronger neural synchronization across participants, which has been linked to higher attention levels [20, 24].

To interpret the weights of the EEG encoders ($\mathbf{w_x}$ in CCA and $\mathbf{W}_s$ in CorrCA), we compute the forward model, which maps the extracted components to the original EEG space [25]. The weights in the forward model reveal how strongly the extracted components are reflected in each EEG channel. The forward models for CCA ($\mathbf{F}_x$) and CorrCA ($\mathbf{F}_s$) are defined as

$$\min_{\mathbf{F}_x} \|\mathbf{X} - \mathbf{X}\mathbf{w_x}\mathbf{F}^{\mathrm{T}}{}_x\|_{\mathrm{F}}^2 \tag{7}$$

[8] Other generalizations of CCA exist, which allow using a different spatial filter for each participant [22, 23]. We opted for CorrCA here because of the limited dataset size, since the reduction in degrees of freedom (i.e. using the same $\mathbf{W}_s$ for all participants) has a regularizing effect on the transformation [23].

and

$$\min_{\mathbf{F}_s} \left\| \begin{bmatrix} \mathbf{X}_1 \\ \vdots \\ \mathbf{X}_N \end{bmatrix} - \begin{bmatrix} \mathbf{X}_1\mathbf{W}_s \\ \vdots \\ \mathbf{X}_N\mathbf{W}_s \end{bmatrix} \mathbf{F}^{\mathrm{T}}{}_s \right\|_{\mathrm{F}}^2, \tag{8}$$

respectively. The solutions to these least-squares problems are given by:

$$\mathbf{F}_x = \mathbf{R}_{xx}\mathbf{w}_{\mathbf{x}} \left(\mathbf{W}^{\mathrm{T}}{}_x\mathbf{R}_{xx}\mathbf{w}_{\mathbf{x}}\right)^{-1}, \tag{9}$$

$$\mathbf{F}_s = \sum_{i=1}^{N} \mathbf{R}_{ii}\mathbf{W}_s \left(\sum_{i=1}^{N} \mathbf{W}^{\mathrm{T}}{}_s\mathbf{R}_{ii}\mathbf{W}_s \right)^{-1}. \tag{10}$$

To prevent our spatial topographies from reflecting overfitted noise in the training set, the covariance matrices $\mathbf{R}_{xx}$ and $\mathbf{R}_{ii}$ are computed using unseen test data.

3.3. Parameters and evaluation

Temporal lag parameters were set according to Yao *et al* [8]. For CCA, we used $L_x = 3$ with $\Delta_x = 1$, capturing EEG information from −33 ms to 33 ms around the current time point, and $L_y = 15$ with $\Delta_y = 0$, capturing video features from approximately 500 ms of history to the current time. For CorrCA, $L_x = 5$ and $\Delta_x = 2$ were used, covering −67 ms to 67 ms.

We adopted leave-one-video-out cross-validation in all experiments. Unless stated otherwise, training was performed on the combined data from all three experimental tasks (54 min per participant: 3 tasks × 6 videos × 3 min). This was an empirical decision, as aggregating data across all tasks yielded better decoding performance than training on individual tasks alone. A possible explanation is that even in Task 1, where participants were instructed to ignore the video, passive visual processing still engages the same neural pathways, providing useful information for estimating the spatial filters. In the stimulus-response correlation analysis, non-fixation periods identified in section 3.1 were excluded from testing, along with a 0.5 s margin selected to outlast saccadic spike potentials (tens of milliseconds [26]) and post-saccadic lambda waves (100–250 ms [27]) while preventing severe data loss, to strictly control for eye-movement confounds. Therefore, the size of the test set varied across tasks and participants. For CorrCA, all data were retained because the proportion of non-fixation samples was small and removing non-fixation periods would disrupt temporal alignment across participants. Test segments were defined as 45 s windows sampled from the test set with overlap, randomly drawn with an average interval of 2 s. The two analyses also treat the marker events of section 2 differently. CorrCA extracts activity that is correlated across participants without knowledge of the stimulus, and because the event timing was identical for all participants, the responses these markers evoke are synchronized across subjects and could inflate the ISC. The surrounding intervals are therefore excluded (section 4.3). CCA instead extracts the component correlated with the object-based optical flow. The event onsets were placed at random with respect to the video content, so the activity they evoke is uncorrelated with that feature and is not extracted by the canonical filters. Therefore, there is no need to discard the corresponding intervals in the match-mismatch (MM) analysis.

For CCA, instead of using raw correlation coefficients, which are rather noisy, we performed MM decoding to quantify stimulus-response coupling strength [28]. Given an EEG segment, the task is to identify the corresponding video segment from two candidates: the correct match and a mismatch (a segment from the same video but different time point). The procedure applies the trained EEG decoder $\mathbf{w}_x$ and video encoder $\mathbf{w}_y$ to compute canonical correlations between the test EEG segment and both candidate video segments. The candidate with the higher sum of the first two canonical correlation components was selected as the predicted match. This decision metric was made *a priori* based on previous studies in neural tracking of natural videos using the same CCA-based methodology [8, 12]. Decoding accuracy was then calculated across all test trials. To assess whether decoding performance was significantly above chance, we circularly permuted the sequence of video segments such that the temporal alignment between EEG and video segments was disrupted and both MM candidates became mismatches (100 permutations per participant). These per-participant permutation results were pooled across all 14 participants to construct a single group-level null distribution comprising 1400 total permutations. The significance bound was set at the 97.5th percentile of this null distribution. Circular permutation was selected for the MM-decoding null because it preserves the marginal statistics and within-segment temporal structure of both the EEG and the video features while destroying only their cross-modal temporal correspondence. Since the mismatch segment was drawn at random for each trial, the resulting decoding accuracies could vary slightly between runs. To obtain stable estimates for the between-task and between-protocol comparisons in section 4, we repeated the full decoding procedure five times and averaged the per-participant accuracies across runs before applying the Wilcoxon signed-rank and Mann–Whitney *U* tests.

For CorrCA, ISC values were computed and averaged across all test segments. Significance was assessed using a permutation test analogous to the MM-decoding null. For each participant, the EEG time series was circularly shifted by a random offset to disrupt the cross-subject temporal alignment while preserving the temporal structure and marginal statistics within each participant's data. ISC was then

recomputed on these permuted data (500 permutations per fold, yielding 3500 total permutations), and the significance threshold was set at the 97.5th percentile of the resulting null distribution, corresponding to a two-sided test with $\alpha = 0.05$.

4. Results

4.1. Effect of eccentricity on decoding performance

Tasks 1 and 2 both had videos gradually moving from center to periphery, differing only in attention condition: participants ignored video content in Task 1 but attended covertly in Task 2. Comparing these two tasks reveals whether attentional modulation persists when the visual objects are not centrally located. Task 3 maintained videos at the center throughout while the participants attended to the content. Comparing Task 3 with Task 2 isolates the effect of eccentricity on decoding performance. MM accuracies for all three tasks are shown in figure 4.

In Task 1, half of the participants (7 out of 14) failed to achieve above-chance decoding accuracy, with a median accuracy of 0.55. Tasks 2 and 3 yielded median accuracies of 0.59 and 0.65, respectively, with most participants achieving significantly above-chance performance. To evaluate the distinct effects of attention and eccentricity, we conducted two comparisons using Wilcoxon signed-rank tests. Because both contrasts tested directional hypotheses specified *a priori* (Task 1 $<$ Task 2 and Task 2 $<$ Task 3), one-sided tests were used, and the two resulting p-values were corrected for multiple comparisons with the Holm–Bonferroni procedure. The Task 1 accuracy was significantly lower than that of Task 2 ($p = 0.032$, $Z = 1.85$, rank-biserial $r = 0.56$; corrected $p_{adj} = 0.048$), confirming that attentional modulation persists even when objects move away from the visual field center. Additionally, Task 2 accuracy was significantly lower than that of Task 3 ($p = 0.024$, $Z = 1.98$, rank-biserial $r = 0.60$; corrected $p_{adj} = 0.048$), demonstrating that shifting the visual stimulus to peripheral locations significantly impairs decoding performance even under identical attentional conditions. This provides direct evidence that eccentricity acts as a confounding factor in visual attention decoding, when neural tracking strength is used to index visual attention. To ensure that this effect is not an artifact of the filters representing a compromise fit between the central and eccentric conditions, we repeated the analysis with filters estimated separately within each task and confirmed that the eccentricity effect persisted (see appendix A.2). Although the corrected p-values lie close to the conventional 0.05 significance threshold, both contrasts remained significant after correction, and the effect sizes (rank-biserial $r = 0.56$ and 0.60) indicate that these are substantial rather than marginal effects. Moreover, we note that this reduction was measured in the neural tracking of object motion. Our design therefore cannot determine whether it is specific to motion processing or reflects a broader decrease in visual stimulus-response coupling at the periphery.

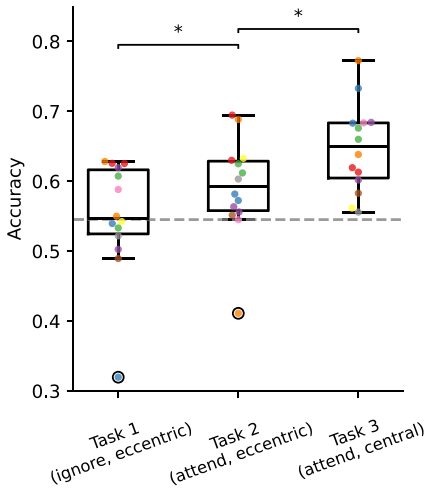


Figure 4. Match-mismatch (MM) decoding accuracy across three experimental tasks on 45 s test segments. Individual participant accuracies are shown as colored dots, with statistical outliers circled (identified by the Tukey 1.5×IQR rule; outliers were retained in all Wilcoxon signed-rank tests). Box plots display median and interquartile range, with whiskers extending to extreme values. The dashed line indicates the significance bound for above-chance performance, defined as the 97.5th percentile of the circular permutation null distribution (1400 permutations; see section 3.3). Asterisks denote significant between-task differences: Task 1 $<$ Task 2 ($p = 0.032$, $Z = 1.85$, rank-biserial $r = 0.56$; corrected $p_{adj} = 0.048$), Task 2 $<$ Task 3 ($p = 0.024$, $Z = 1.98$, rank-biserial $r = 0.60$; corrected $p_{adj} = 0.048$), demonstrating both attentional effects and eccentricity confounds.

4.2. Gaze fixation versus free viewing

In this section, we compared the decoding performance under our gaze-fixation protocol with previous free-viewing studies. Using the free-viewing dataset from Yao *et al* [8][9], we selected only the data corresponding to the same video stimuli used in our current study, yielding 21 min per participant (for both datasets). EOG data were linearly regressed out from EEG during preprocessing, as in the present dataset. For fair comparison, only the data from Task 3 (attention condition with object in the center) were used from the current study in both training and testing to have an equal amount of test and train data, and to remove effects of eccentricity. The same leave-one-video-out cross-validation was performed. Results are presented in figure 5.

The gaze-fixation protocol yielded a mean accuracy of 0.62, compared to 0.67 for free viewing. To test whether this reduction was significant, we used a Mann–Whitney U test since the participant groups differed between the two protocols. The p-value was

[9] The original study included 20 subjects, with 19 consenting to make their data publicly available in [29].

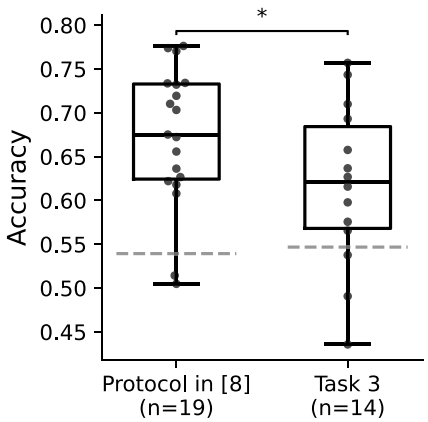


Figure 5. Comparison of match-mismatch (MM) decoding accuracy on 45 s test segments under free-viewing (19 participants, [8, 29]) and gaze-fixation (14 participants) protocols. Dots represent the accuracies of individual participants. Box plots display median and interquartile range, with whiskers extending to extreme values. The dashed lines indicate the significance bound for above-chance performance for each protocol, defined as the 97.5th percentile of the circular-permutation null distribution (calculated using 100 permutations per participant, yielding 1900 total permutations for the protocol in [8] and 1400 for the current gaze-fixation protocol; see section 3.3). Gaze fixation significantly reduced decoding accuracy compared to free viewing (Mann–Whitney U test, $p = 0.042$, $U = 181.0$, rank-biserial $r = 0.36$).

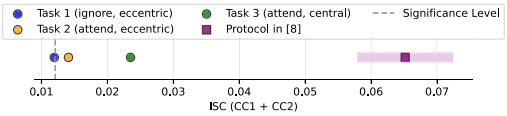


Figure 6. Sum of the inter-subject correlations (ISCs) of the first two canonical components across experimental conditions. ISC values are computed separately for each task under the gaze-fixation protocol and compared with the free-viewing protocol. To match the participant count of the current study, the free-viewing reference is generated by repeatedly drawing 14 participants at random from the original dataset [8, 29] (5 independent draws) and computing the ISC for each draw. The shaded region represents the standard deviation across these draws and the square represents the mean. The vertical dashed line marks the significance threshold, defined as the 97.5th percentile of the circular permutation null distribution (500 permutations per fold, totaling 3500; see section 3.3).

0.042 ($U = 181.0$, rank-biserial $r = 0.36$), suggesting significant performance loss under gaze fixation. We note that the results in figure 5 differ from the Task 3 results shown in figure 4, which is due to the difference in the amount of training data in both analyses (the results in figure 4 use 3 times more training data, as training data is aggregated across the 3 tasks).

4.3. Effect on group analysis

The previous sections investigated the stimulus-response coupling on a per-subject basis. In this section, we performed a group analysis based on the ISC to investigate the coherence of the neural responses across participants, without explicitly linking these to the stimulus signal. We computed ISCs for all three tasks in the current protocol, excluding time points from −250 ms to 500 ms relative to the onset of the artificially added markers (fading of the fixation cross and red circle), irrespective of whether the task required a response to them, to avoid contamination from event-evoked and motor responses that are time-locked and therefore synchronized across participants. The results are shown in figure 6, alongside the free-viewing protocol results from [8] for comparison. The free-viewing results were computed by randomly selecting 14 participants (repeated 5 times) from the original dataset [8, 29] to match the current study's participant count, as the number of participants influences the ISC values. As in section 4.2, only data corresponding to the same video stimuli as in the current gaze-fixation protocol were used, yielding 18×14 min of training data per fold. Note that this was only one-third of the training data available in the gaze-fixation protocol, where data from all three tasks were aggregated for training.

The ISC pattern mirrored the decoding accuracy trends from section 4.1: Task 1 showed the lowest ISC (slightly below significance threshold), followed by Task 2, with Task 3 exhibiting the highest ISC. This confirmed both attention- and eccentricity-related attenuation of the stimulus-evoked neural responses, reducing the ISC across participants. However, Task 2 ISC was only marginally above significance, showing a larger gap with Task 3 than with Task 1. This suggests that eccentricity may have an even stronger impact on ISC than attention effects. Additionally, free-viewing protocol results were substantially higher despite a smaller training data size, which aligns with the different decoding performance observed in section 4.2.

4.4. Spatial topographies of the decoding models

To gain insights into the neural sources contributing to the decoding performance and ISC, we computed the forward models for both CCA and CorrCA components using (9) and (10), respectively. To avoid introducing noise, only the forward models corresponding to significant results across folds were retained and averaged. For CCA, we averaged the forward models across all participants to generate the spatial topography of the first component, which exhibited the largest stimulus-response correlation. For CorrCA, we visualized the forward model of the group decoder that yielded the highest ISC. Because canonical components have an arbitrary polarity, the per-participant forward models were sign-aligned prior to averaging. Therefore, only the spatial weighting pattern and not its absolute polarity should be interpreted. The resulting spatial topographies for the different tasks are shown in figure 7.

Across all topographies, we observed no strong activation in the frontal channels (relative to other regions), indicating that eye-movement artifacts,

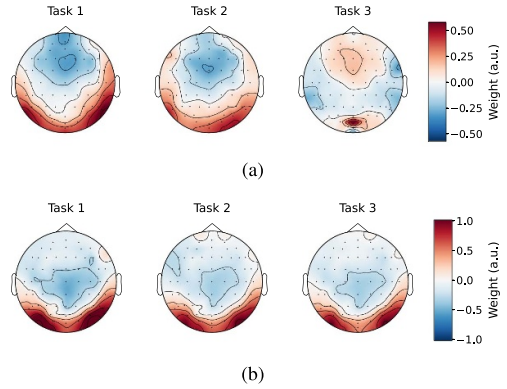


Figure 7. Spatial topographies (forward models) of the decoding models for each task. (a) CCA: forward model of the most strongly correlated canonical component, averaged across participants. (b) CorrCA: forward model of the component with the highest ISC. Since the polarity of each component is arbitrary, only the spatial pattern is interpretable.

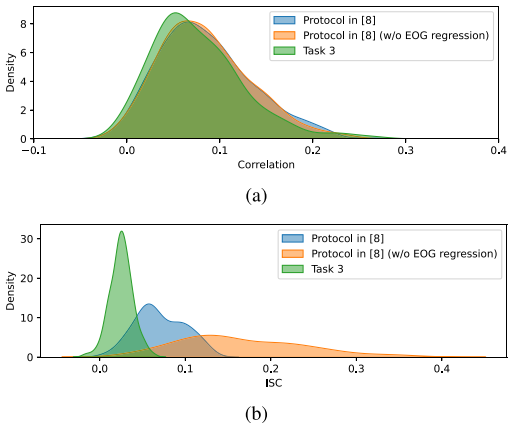


Figure 8. Distributions of (a) stimulus-response correlations and (b) inter-subject correlations across participants for 45 s segments under the free-viewing and gaze-fixation protocols. The values represent the sum of the first two components. For comparison, results obtained from EEG without EOG regression are also included. For the gaze-fixation condition, only Task 3 (attend, central) is shown. Curves are Gaussian kernel density estimates computed from approximately 500 45 s segments (pooled across participants) for (a), and 100 45 s segments for (b). The bandwidth was selected automatically by Scott's rule, the default of seaborn's kdeplot.

which were at least partially removed using EOG regression (see section 3.1), probably contributed minimally to decoding performance and ISC. Beyond this shared absence of frontal involvement, the topographies differed systematically across tasks and between the two decoding methods. We interpret these patterns and their link to the eccentricity effect in section 5.4.

5. Discussion

5.1. Group analysis is more susceptible to eye movement artifacts than stimulus-response analysis

From figure 6, we observed that the decrease in ISC from free-viewing to gaze-fixation protocols appeared more pronounced than the corresponding decrease in decoding accuracy shown in figure 5. However, note that figure 5 displays MM accuracy, whereas ISC is a correlation metric. To more directly compare the effects of gaze fixation on group-level and individual-level analyses, we plotted the distributions of stimulus-response correlations (aggregated across participants) and ISCs in figure 8 for both the free-viewing protocol and the gaze-fixation protocol (Task 3: attend, central). For reference, we also included results obtained without EOG regression under the free-viewing protocol.

For the individual stimulus-response analysis, the distributions with and without EOG regression under the free-viewing protocol overlapped substantially. Under the gaze-fixation protocol (with EOG regression), the distribution shifted slightly leftward with a thinner right tail, indicating that gaze fixation reduced stimulus-response correlations rather mildly. In contrast, the group analysis showed a much stronger effect. After regressing out EOG, the free-viewing ISC distribution already exhibited a pronounced leftward shift, indicating that EOG-capturable ocular artifacts contributed substantially to ISC. Under the gaze-fixation protocol, ISC values decreased further and the distribution became narrower. This additional reduction beyond EOG regression may be partially attributed to the absence of neural activities such as motor signals from saccade planning and execution that are not captured by EOG channels but are nonetheless synchronized across participants viewing the same dynamic content. Moreover, standard EOG regression is unable to remove saccadic spike potentials, lambda waves, and gaze-induced visual motion, all of which act coherently across participants to inflate ISC under free-viewing conditions. Together, these results suggest that group analysis is more susceptible to eye-movement confounds than individual stimulus-response analysis.

One likely reason is that eye movements tend to be synchronized across participants when viewing the same dynamic visual stimuli, artificially inflating ISC. Stimulus-response analysis, on the other hand, focuses on the relationship between the stimulus and each participant's neural response. Although eye-movement-related activity in the EEG can also contribute to stimulus-response correlations when using motion-based video features, its impact is less pronounced, likely because the relationship between the stimulus and eye movements is indirect and more difficult to capture.

5.2. Why does gaze fixation reduce decoding accuracy and ISC?

While gaze fixation clearly reduces decoding accuracy and ISC, as shown in sections 4.2 and 4.3, the underlying mechanisms remain unclear. The reduction could arise from the loss of synchronized eye-movement information that aids decoding and boosts ISC in free-viewing paradigms, and/or from the increased difficulty of maintaining sustained attention when gaze is constrained. The covert attention paradigm used here, while necessary to control for eye movement confounds, is less naturalistic than overt attention, where eye movements naturally accompany and facilitate engagement. This reduced ecological validity, combined with increased cognitive demand, may also contribute to weaker neural responses. Indeed, most participants reported that maintaining fixation while attending to moving objects was challenging. However, since the ground truth of a participant's actual attentional state is unavailable, disentangling these two factors is impossible here.

5.3. Free-viewing studies likely rely on genuine neural responses to object motion

In previous free-viewing studies that explicitly addressed eye-movement confounds [8, 12], several analyses were conducted to demonstrate that the observed stimulus-response correlations and above-chance decoding accuracies were not solely driven by eye movement artifacts. These included regressing out EOG signals, restricting analyses to EEG channels less affected by eye movements, and removing data segments containing saccades. Together, these approaches provide strong evidence that EEG-based decoding of visual attention captures genuine neural responses to object motion. However, since it was never possible to completely rule out all eye-movement confounds in free-viewing paradigms, some uncertainty remained.

In the present study, strict gaze fixation was imposed to directly eliminate eye-movement confounds. The fact that significant decoding accuracy and ISC persisted under these conditions provides additional support that previous free-viewing results at least partially reflect genuine neural responses to object motion, although the between-cohort nature of the free-viewing/gaze-fixation comparison precludes quantifying the exact proportion attributable to motion-related neural activity. Future work utilizing a within-subjects design, which evaluates the same participants under both free-viewing and fixation conditions, will be necessary to directly quantify these relative contributions to decoding accuracy.

5.4. Task and method-dependent variations in spatial topographies

Beyond the shared absence of frontal involvement noted in section 4.4, the topographies varied with both task and decoding method. For CCA, Tasks 1 and 2 yielded similar topographies with broadly distributed occipital and posterior-temporal weights. This suggests that the same stimulus-driven neural sources were engaged despite differing attention conditions. Task 3, however, showed a different topography with focal occipital weights. This eccentricity-dependent reorganization of the scalp topography aligns with recent and foundational visual evoked potential studies [30–32], which demonstrated that the occipital response is midline-symmetric for foveal stimuli but shifts toward the contralateral hemisphere as the stimulus moves peripherally. Because leftward and rightward video displacements in our paradigm were randomized across videos, averaging the forward models superimposes these oppositely lateralized peripheral sources. This superposition explains why the eccentric Tasks 1 and 2 exhibit broader, more bilaterally distributed occipital and posterior-temporal weights compared to the centrally located Task 3.

In contrast, the CorrCA topographies were highly consistent across all tasks, dominated by broadly distributed occipital-temporal weights. It is important to note that EEG components extracted by CCA were steered to maximize the correlation with the object-based optical flow feature, while CorrCA components were steered to maximize ISC across participants, which inherently captures a broader mixture of shared neural responses. As pointed out in [8], the object-based optical flow feature used in CCA only explains a small portion of inter-subject covariance in EEG, indicating that the remaining covariance may be dominated by other shared neural responses to the video. The consistent broad activation in the occipital-temporal region across all tasks could reflect engagement of specific networks like those for face and body perception [33], or the extraction of other conceptual information during naturalistic action viewing [34]. Attention and eccentricity may simply scale the magnitude of this shared response, resulting in the consistent topography across tasks.

5.5. What a behavioral record could and could not have established

The key presses in the event detection tasks were not logged (section 2.2), so neither detection accuracy nor reaction times are available. Two limitations follow: we cannot report whether individual participants complied with the vigilance instructions, and we cannot identify erroneous responses.

Such a record would not, however, have indexed attention to the video content, which is the quantity our analyses concern. In Task 1, a participant could report every dimming of the cross while still covertly following the performer throughout. In Tasks 2 and 3, detecting the fading circle shows that the video region was being monitored, but not necessarily that attention was directed to the video content, even though the circle was kept subtle (section 2.2)

precisely to prevent this. The subtlety also creates the opposite problem: a circle could be missed by a participant who was fully engaged with the video, and that miss would be misread as inattention. This is why we treated the vigilance tasks as a manipulation rather than a measure.

Quantifying it would require a different kind of behavioral record. One option is to probe the video content directly after each block, for instance by asking how many rotations the performer made. Such a task can, evidently, not be used in the ignore condition. Ensuring that the video content is genuinely ignored would instead call for a task more demanding than cross-dimming detection, such as a difficult auditory or arithmetic task, where a high score would indicate that the participant was occupied by that task and had little capacity left for the video. Measures of this kind remain indirect, and establishing a ground truth for the attentional state is inherently difficult.

Returning to the behavioral task in this study, other information would also be useful if the keypress record were available. For instance, reaction times to visual events could hint at whether participants built up anticipation of those events. However, because our analyses are not event-based, and the missing record concerns only the marker events, our results and overarching conclusions are not substantially affected. In MM decoding, the marker events are uncorrelated with the optical-flow feature that drives the decoding (section 3.3), and in ISC analysis, the marker intervals are excluded entirely.

6. Conclusion

This study revealed a spatial confound in EEG-based visual attention decoding by manipulating stimulus eccentricity under gaze fixation. When objects moved toward peripheral locations, lower decoding accuracies and lower ISCs were observed, demonstrating that peripheral objects are more difficult to decode than central objects. This spatial confound represents an important limitation for current attention decoding approaches that assume coupling strength reflects attention levels alone. Comparison with free-viewing conditions showed that gaze fixation reduced both decoding accuracy and ISC, yet both measures remained statistically significant. The latter suggests that neural tracking of video motion still exists and is modulated by attention under strict gaze fixation, and that previous free-viewing studies also partially reflect genuine neural responses to object motion and not only gaze-induced components such as residual EOG artifacts, gaze-related motor neural activity, or gaze shift-evoked neural responses. While our sample size ($N = 14$) is relatively small, the observed attention and eccentricity effects were consistent across both individual-level stimulus-response analysis and group-level ISC analysis, lending confidence to the robustness of our findings.

Acknowledgments

This research is funded by the Research Foundation—Flanders (FWO) Project Nos. G081722N and G026026N, junior postdoctoral fellowship fundamental research of the FWO (for S. Geirnaert, 1242524 N), Internal Funds KU Leuven (Projects IDN/23/006, C14/25/108, C3/25/107, and METH/24/003), and the Flemish Government (AI Research Program). Y. Yao, S. Geirnaert, T. Tuytelaars and A. Bertrand are also affiliated with Leuven. AI—KU Leuven institute for AI, Belgium.

Data availability statement

The data that support the findings of this study will be openly available following an embargo at the following URL/DOI: https://doi.org/10.48804/5PBGIY. Data will be available from 1 October 2026.

Appendix

A.1. Task and video presentation order

The task and video presentation order for each participant is shown in table 3. Task 1 (ignore, eccentric) was presented first for 3 participants, second for 4, and third for 7; Task 2 (attend, eccentric) first for 6, second for 6, and third for 2; and Task 3 (attend, central) first for 5, second for 4, and third for 5. Within each task block, the video orders were well distributed: across the 42 blocks all orderings were unique, each video appeared in early, middle, and late positions roughly equally often (mean serial position 3.6–4.5, against a midpoint of 4.0), and no video tended systematically to precede any other.

A.2. Per-condition estimation of the spatial filters

In the main analysis (section 4.1), a single set of CCA filters was estimated from the combined recordings of all three tasks and then reused to decode the held-out segments of each individual task (section 3.3). Since every condition is decoded through the same filters, the comparisons between tasks favor none of them. One may nonetheless ask whether the ranking of the tasks is sensitive to how the filters are obtained: a filter learned from a blend of central and eccentric recordings is a compromise solution that may fit the central and the eccentric conditions to differing degrees. To examine this, we re-estimated the filters separately for Tasks 2 and 3. For each task, a dedicated filter was learned and tested only on the recordings of

Table 3. Task-block order and within-block video presentation order for each participant ($N = 14$). Within each block, the comma-separated numbers are video IDs.

Participant	1st block	2nd block	3rd block
1	Task 3: 12, 08, 05, 16, 07, 04, 14	Task 1: 05, 14, 16, 08, 04, 07, 12	Task 2: 12, 05, 07, 08, 16, 14, 04
2	Task 2: 08, 07, 12, 05, 14, 04, 16	Task 1: 16, 07, 05, 08, 14, 12, 04	Task 3: 12, 14, 05, 16, 04, 07, 08
3	Task 2: 12, 16, 04, 05, 07, 14, 08	Task 1: 04, 12, 07, 14, 16, 08, 05	Task 3: 08, 12, 14, 07, 05, 16, 04
4	Task 3: 05, 08, 04, 12, 07, 16, 14	Task 2: 07, 04, 14, 05, 08, 16, 12	Task 1: 16, 08, 12, 05, 07, 04, 14
5	Task 2: 04, 05, 16, 14, 07, 12, 08	Task 3: 16, 07, 05, 08, 12, 14, 04	Task 1: 08, 04, 05, 12, 14, 07, 16
6	Task 2: 12, 04, 05, 07, 16, 14, 08	Task 3: 05, 08, 14, 16, 07, 12, 04	Task 1: 14, 05, 04, 12, 07, 16, 08
7	Task 3: 07, 05, 14, 08, 04, 16, 12	Task 1: 07, 04, 12, 08, 14, 05, 16	Task 2: 05, 08, 14, 04, 12, 16, 07
8	Task 3: 12, 05, 07, 14, 16, 08, 04	Task 2: 08, 14, 04, 16, 07, 05, 12	Task 1: 05, 07, 04, 16, 14, 12, 08
9	Task 1: 04, 08, 16, 05, 12, 07, 14	Task 2: 14, 16, 12, 07, 05, 04, 08	Task 3: 14, 12, 07, 16, 05, 04, 08
10	Task 1: 14, 07, 16, 05, 04, 08, 12	Task 2: 07, 14, 12, 04, 16, 08, 05	Task 3: 16, 12, 07, 08, 05, 14, 04
11	Task 3: 07, 12, 08, 04, 14, 05, 16	Task 2: 12, 07, 16, 04, 08, 14, 05	Task 1: 14, 05, 04, 16, 07, 12, 08
12	Task 2: 12, 08, 05, 16, 07, 14, 04	Task 3: 07, 14, 05, 16, 08, 04, 12	Task 1: 05, 14, 12, 08, 16, 07, 04
13	Task 2: 07, 04, 08, 16, 12, 14, 05	Task 3: 14, 08, 12, 05, 07, 16, 04	Task 1: 08, 05, 12, 04, 14, 07, 16
14	Task 1: 04, 07, 14, 16, 12, 08, 05	Task 2: 12, 07, 14, 16, 04, 05, 08	Task 3: 12, 16, 08, 07, 04, 14, 05

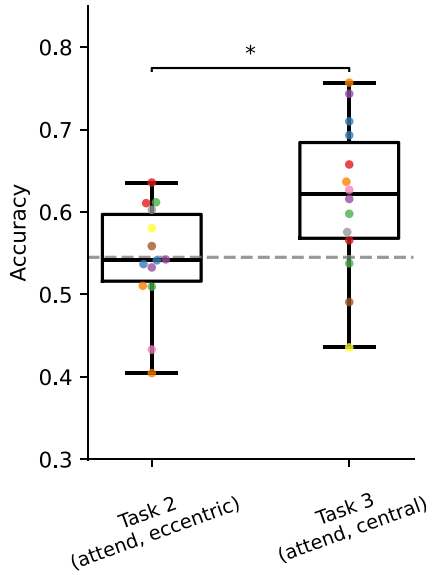


Figure 9. Match-mismatch (MM) decoding accuracy for the attend-eccentric (Task 2) and attend-central (Task 3) conditions on 45 s test segments, obtained with CCA spatial filters estimated separately within each task. This differs from figure 4, where the filters are estimated from the combined data of all three tasks. Individual participant accuracies are shown as colored dots, with statistical outliers circled (identified by the Tukey 1.5×IQR rule; outliers were retained in all Wilcoxon signed-rank tests). Box plots display the median and interquartile range, with whiskers extending to extreme values. The dashed line indicates the significance bound for above-chance performance, defined as the 97.5th percentile of the circular permutation null distribution recomputed for the present per-condition decoders (1400 permutations). The asterisk denotes a significant difference between tasks (Wilcoxon signed-rank test, $p = 0.028$, $Z = 1.91$, rank-biserial $r = 0.58$). Task 3 accuracy exceeds Task 2 accuracy, confirming that the eccentricity effect persists under within-task filter estimation.

that same task, again with leave-one-video-out cross-validation, so that the decoder for each condition was derived exclusively from that condition's own data. This variant draws on a third of the training material used in the main analysis, so the resulting accuracies are inevitably lower (figure 9). What matters here is therefore the relative ordering of Tasks 2 and 3 rather than the absolute accuracy levels.

Even under this stricter, condition-specific estimation, decoding accuracy for the central condition (Task 3) remained above that for the eccentric condition (Task 2) (Wilcoxon signed-rank test, $p = 0.028$, $Z = 1.91$, rank-biserial $r = 0.58$). The eccentricity effect from section 4.1 thus holds under an entirely independent estimation scheme, showing that the weaker neural tracking of motion at peripheral locations originates in the neural responses themselves and is not an incidental by-product of how the spatial filters were learned.

ORCID iDs

Yuanyuan Yao 0000-0002-4307-8137
Simon Geirnaert 0000-0002-4120-4232
Céline R Gillebert 0000-0001-6686-7262
Tinne Tuytelaars 0000-0003-3307-9723
Alexander Bertrand 0000-0002-4827-8568

References

[1] Thiele A and Bellgrove M A 2018 Neuromodulation of attention *Neuron* **97** 769–85
[2] Hillyard S A and Anllo-Vento L 1998 Event-related brain potentials in the study of visual selective attention *Proc. Natl Acad. Sci.* **95** 781–7
[3] Lalor E C, Kelly S P, Pearlmutter B A, Reilly R B and Foxe J J 2007 Isolating endogenous visuo-spatial attentional effects using the novel visual-evoked spread spectrum analysis (vespa) technique *Eur. J. Neurosci.* **26** 3536–42
[4] Lalor E C, Power A J, Reilly R B and Foxe J J 2009 Resolving precise temporal processing properties of the auditory system using continuous stimuli *J. Neurophysiol.* **102** 349–59
[5] Mesgarani N and Chang E F 2012 Selective cortical representation of attended speaker in multi-talker speech perception *Nature* **485** 233–6
[6] Baldauf D and Desimone R 2014 Neural mechanisms of object-based attention *Science* **344** 424–7

[7] Dmochowski J P, Ki J J, DeGuzman P, Sajda P and Parra L C 2018 Extracting multidimensional stimulus-response correlations using hybrid encoding-decoding of neural activity *Neuroimage* **180** 134–46
[8] Yao Y, Stebner A, Tuytelaars T, Geirnaert S and Bertrand A 2024 Identifying temporal correlations between natural single-shot videos and EEG signals *J. Neural Eng.* **21** 016018
[9] Li T, Geirnaert S, Broek D V de, Bellon E, De Smedt B and Bertrand A 2025 Temporal variation in the acoustic dynamic range is a confounding factor in EEG-based tracking of absolute auditory attention to speech *2025 47th Annual Int. Conf. IEEE Engineering in Medicine and Biology Society (EMBC)* pp 1–4
[10] Corbetta M and Shulman G L 2002 Control of goal-directed and stimulus-driven attention in the brain *Nat. Rev. Neurosci.* **3** 201–15
[11] Itti L and Koch C 2001 Computational modelling of visual attention *Nat. Rev. Neurosci.* **2** 194–203
[12] Yao Y, De Swaef W, Geirnaert S and Bertrand A 2025 EEG-based decoding of selective visual attention in superimposed videos *IEEE J. Biomed. Health Inform.* **29** 7248–61
[13] Curcio C A, Sloan K R, Kalina R E and Hendrickson A E 1990 Human photoreceptor topography *J. Comput. Neurol.* **292** 497–523
[14] Strasburger H, Rentschler I and Jüttner M 2011 Peripheral vision and pattern recognition: a review *J. Vis.* **11** 13–13
[15] Wang B, Guo J, Yan T, Ohno S, Kanazawa S, Huang Q and Wu J 2016 Neural responses to central and peripheral objects in the lateral occipital cortex *Front. Hum. Neurosci.* **10** 54
[16] Ki J J, Dmochowski J P, Touryan J and Parra L C 2021 Neural responses to natural visual motion are spatially selective across the visual field, with selectivity differing across brain areas and task *Eur. J. Neurosci.* **54** 7609–25
[17] Müller M M, Malinowski P, Gruber T and Hillyard S A 2003 Sustained division of the attentional spotlight *Nature* **424** 309–12
[18] He K, Gkioxari G, Dollár P and Girshick R 2017 Mask R-CNN *Proc. IEEE In. Conf. on Computer Vision* pp 2961–9
[19] Schubert E, Sander J, Ester M, Kriegel H P and Xu X 2017 Dbscan revisited, revisited: why and how you should (still) use dbscan *ACM Trans. Database Syst. (TODS)* **42** 1–21
[20] Dmochowski J P, Sajda P, Dias J and Parra L C 2012 Correlated components of ongoing EEG point to emotionally laden attention–a possible marker of engagement? *Front. Hum. Neurosci.* **6** 112
[21] Hotelling H 1992 *Breakthroughs in Statistics: Methodology and Distribution* (Springer) pp 162–90
[22] Kettenring J R 1971 Canonical analysis of several sets of variables *Biometrika* **58** 433–51
[23] Geirnaert S, Yao Y, Francart T and Bertrand A 2025 Stimulus-informed generalized canonical correlation analysis for group analysis of neural responses to natural stimuli *IEEE J. Biomed. Health Inform.* **29** 970–83
[24] Ki J J, Kelly S P and Parra L C 2016 Attention strongly modulates reliability of neural responses to naturalistic narrative stimuli *J. Neurosci.* **36** 3092–101
[25] Haufe S, Meinecke F, Görgen K, Dähne S, Haynes J-D, Blankertz B and Bießmann F 2014 On the interpretation of weight vectors of linear models in multivariate neuroimaging *Neuroimage* **87** 96–110
[26] Keren A S, Yuval-Greenberg S and Deouell L Y 2010 Saccadic spike potentials in gamma-band EEG: characterization, detection and suppression *Neuroimage* **49** 2248–63
[27] Brigo F 2011 Lambda waves *Am. J. Electroneurodiagn. Technol.* **51** 105–13
[28] De Cheveigné A, Slaney M, Fuglsang S A and Hjortkjaer J 2021 Auditory stimulus-response modeling with a match-mismatch task *J. Neural Eng.* **18** 046040
[29] Yao Y, Stebner A, Tuytelaars T, Geirnaert S and Bertrand A 2024 Video-EEG encoding-decoding dataset KU Leuven (https://doi.org/10.5281/zenodo.10512414)
[30] Phangwiwat T, Phunchongharn P, Wongsawat Y, Chatnuntawech I, Wang S, Chunharas C, Sprague T C, Woodman G F and Itthipuripat S 2024 Sustained attention operates via dissociable neural mechanisms across different eccentric locations *Sci. Rep.* **14** 11188
[31] Mohr K S, Geuzebroek A C and Kelly S P 2024 Visual cortical area contributions to the transient, multifocal and steady-state VEP: a forward model-informed analysis *Imaging Neurosci.* **2** imag–2–00152
[32] Di Russo F, Martínez A, Sereno M I, Pitzalis S and Hillyard S A 2002 Cortical sources of the early components of the visual evoked potential *Hum. Brain Mapp.* **15** 95–111
[33] Meeren H K M, Gelder B de, Ahlfors S P, Hämäläinen M S and Hadjikhani N 2013 Different cortical dynamics in face and body perception: an meg study *PLoS One* **8** 1–13, 09
[34] Dima D C, Culham J C and Mohsenzadeh Y 2026 Distinct perceptual and conceptual representations of natural actions along the lateral and dorsal visual streams *Commun. Biol.* **9** 577